Land-to-sea indicators of the Zanclean megaflood

Check for updates

Aaron Micallef [1] ✉, Giovanni Barreca[2,3,4], Christian Hübscher [5], Angelo Camerlenghi [6], Paul Carling [7], Jose Maria Abril Hernandez [8], Raúl Periáñez [8], Daniel Garcia-Castellanos[9], Jonathan Ford [6], Benedikt Haimerl [5], Matthias Hartge [5], Jonas Preine [5] & Antonio Caruso [10]

One debated scenario for the termination of the Messinian salinity crisis 5.33 million years ago is cataclysmic refilling of the Mediterranean Sea through the Zanclean megaflood. Here we present a clear line of onshore-to-offshore evidence for this megaflood spilling over a shallow-water marine corridor in south-east Sicily into the nearby subaqueous Noto Canyon: (i) >300 asymmetric and streamlined erosional ridges aligned with the megaflood direction, (ii) poorly-sorted breccia deposited between the Messinian and Lower Zanclean Trubi Formations, (iii) soft-sediment deformation structures and clastic injections in the breccia and underlying units, and (iv) a 20 kilometre wide erosional shelf channel connecting the ridges with Noto Canyon. Numerical modelling results support the modulation of flow velocity and direction by the excavation of the channel and Noto Canyon. Our findings demonstrate that the Messinian salinity crisis was terminated through a cataclysmic flood, which implies pronounced Mediterranean sea-level drawdown prior to the flooding.

Between 5.97 and 5.33 million years ago (Ma), the Mediterranean Sea underwent a period of isolation from the global ocean - the Messinian salinity crisis (MSC) - allegedly leading to a km-scale sea-level drawdown and widespread salt deposition[1–5]. The ≈1 km³ volume of resulting evaporitic rocks[6,7] sequestered ≈5% of the global ocean salts, which implies that during the MSC there was an intermittent influx of Atlantic waters supplying the necessary ions for salt deposition, in addition to the ions contributed by river runoff[8]. The return to fully stable marine conditions at the end of the MSC was initially seen as a gradual process taking place through a waterfall across the Strait of Gibraltar. Although a "geologically instantaneous" flood was foreseen[9], the duration of the refill was estimated at as much as 10 ka[10]. The cataclysmic scenario for the end of the crisis gained support from seismic reflection data revealing an erosion channel stretching from the Gulf of Cadiz (Atlantic Ocean) to the Alboran Sea, which suggested that a single-stage flooding event - known as the Zanclean megaflood— refilled the Mediterranean[11,12]. This megaflood is thought to have been caused by overtopping Atlantic waters through a Late Messinian isthmus near the modern Gibraltar Strait, which initially filled the western Mediterranean, and subsequently spilled over the intrabasinal Sicily Sill, filling the eastern Mediterranean. Estimates suggest that the megaflood's discharge and duration ranged from 68 to 100 Sverdrups (Sv = 1 million m³ s⁻¹), and between 2 and 16 years, respectively; the peak discharge and water velocity likely occurred during the overspill across the Sicily Sill[11,13,14]. The dimensions of the inferred Zanclean megaflood would make it the largest known flooding event on Earth, one to two orders of magnitude larger than well-documented Pleistocene events induced by the northern hemisphere ice-sheet disintegration[15,16], and one of the largest known in the solar system[11].

The megaflood hypothesis is supported by a number of observations. In both outcrop and drill samples, a sharp lithological and palaeontological boundary marks the transition from shallow, non-marine sediments to overlying deep, open marine water deposits[17,18], whereas sapropels point to a substantial transfer of salt from the western to the eastern Mediterranean[19]. Erosional and depositional features associated with the megaflood include a buried 390 km long channel and 35 km long megabars near the Strait of Gibraltar[20,21]. In the western Ionian Basin, a 1500 km³ chaotic sedimentary deposit lies buried to the east of Noto Canyon, an exposed theatre-shaped canyon carved into the Malta Escarpment[22,23]. Additionally, in southwest Sicily, a 5–7 m thick sandy contouritic deposit is interpreted to have formed

[1]Monterey Bay Aquarium Research Institute, Moss Landing, CA, USA. [2]Dipartimento di Scienze Biologiche, Geologiche e Ambientali, Università di Catania, Catania, Italy. [3]CRUST—Interuniversity Centre for 3D Seismotectonics with Territorial Applications, Chieti, Italy. [4]Istituto Nazionale di Geofisica e Vulcanologia, Osservatorio Etneo, Italy. [5]Institut für Geophysik, Universität Hamburg, Bundesstraße 55, 20146 Hamburg, Germany. [6]National Institute of Oceanography and Applied Geophysics–OGS, Borgo Grotta Gigante 42/C, 34010 Sgonico, Trieste, Italy. [7]Geography & Environmental Science, University of Southampton, Southampton, UK. [8]Dpto. Física Aplicada I ETSIA, Universidad de Sevilla, Ctra. Utrera km 1, Sevilla, 41013, Spain. [9]Geosciences Barcelona, Geo3BCN-CSIC, Barcelona, Spain. [10]Dipartimento di Scienze e Tecnologie Biologiche Chimiche e Farmaceutiche (STEBICEF), Università degli studi di Palermo, via Archirafi 18, 90123 Palermo, Italy. ✉e-mail: amicallef@mbari.org

by bottom currents during the reconnection of isolated water bodies[24]. Direct access to these locations has been limited to just a few drilling sites, and the megaflood hypothesis remains subject to debate[25–27]. Several of the cited studies encountered limitations, including lack of a robust age model, ambiguous geophysical data interpretation, and modelling that relies on low-resolution topographic data and poorly constrained palaeogeography. Alternative scenarios have also been proposed for the termination of the MSC. These scenarios include infilling by an overspill of Paratethyan (former Black Sea) water followed by Atlantic inflow once the Mediterranean Basin was refilled[28], or by Atlantic seawater restoring normal open marine conditions in an evaporitic basin that was not subject to substantial sea-level drawdown[4]. Validation of the Zanclean megaflood hypothesis requires directly characterising the evidence left by the passage of flooding waters in terms of geomorphology, sedimentology, and stratigraphy. Here we report direct onshore evidence of megaflood erosional and depositional indicators, preserved as subaerial rock outcrops in SE Sicily, along with geophysical imaging of a buried erosional channel in the continental shelf offshore. Supported by numerical modelling of the flow, our shoreline-crossing field evidence confirms that a cataclysmic megaflood overtopped the Sicily Sill at the termination of the MSC. We are thereby able to constrain the evolution of the flow direction, depth, velocity, and shear stress of the Zanclean megaflood in the central Mediterranean region.

The intrabasinal Sicily Sill in SE Sicily (Fig. 1b) is part of the Hyblean foreland domain, the northernmost promontory of the African continental plate[29]. Positioned about 60 km SE from the front of the Sicilian Fold and Thrust Belt (Fig. 1a), the geology and geomorphology of the sill remain poorly characterised. The sill comprises a NE-SW trending, 13 km-wide depressed region that underwent tectonic extension and subsidence during the Miocene. Since the Pliocene, the sill has been uplifted together with the Hyblean Plateau[29], and presently lies at an elevation of no more than 120 m above sea-level (Fig. 1b). The lithological framework of the sill consists of a thick, middle-upper Miocene, open shelf to shallow water sedimentary sequence, which is unconformably covered by pelagic chalk deposits of Zanclean age[30] and breccia. Messinian evaporites crop out locally. The continental margin east of the Sicily Sill features a 12 km wide shelf. The shelf leads eastward to the 3 km high carbonate cliff of the Malta Escarpment, which hosts the 6 km wide submarine Noto Canyon[31]. The theatre-shaped head of the Noto Canyon had been suggested to reflect erosion of the Malta Escarpment by the Zanclean megaflood[22].

Results

Ridge morphometry

The central part of the sill is dominated by >300 ridges spread across an 8–10 km wide corridor (Fig. 1b). At their base they have a mean length (L) of 640 m (σ = 554 m) and a mean width (W) of 360 m (σ = 250 m). Their mean relief is 40 m (σ = 28 m). The overall circular mean direction of the long axes of ridge tops and bases is 40° (Fig. 2a). With respect to the mean direction, the majority of ridges are asymmetric in vertical sections along each long axis, with lee sides steeper than the stoss sides (Fig. 2d). In plan view, many ridge tops display aspect ratios (W/L) of 0.27 (Fig. 2c), which is commensurate with streamlining[32–35]. Although some ridge bases do have aspect ratios approaching 0.27, the majority are less-well streamlined and elongated (aspect ratio of 0.49; Supplementary Fig. 3). Ridges tend to become more streamlined for shorter lengths and lower heights (Supplementary Fig. 4). Shorter, lower and more streamlined ridges occur in the SE-half of the study area, whilst longer, higher and less streamlined ridges are located in the NW (Fig. 2b).

Ridge outcrops, age and deformation structures

A breccia unit is preserved along the top of most elongated ridges (Fig. 3a–c). The outcrops of the unit are up to 8 m thick and their lateral continuity never exceeds a few tens of metres. Breccia is primarily poorly sorted and clast-supported. Rarely, it is a well sorted, clast-supported breccia, or a poorly sorted, matrix-supported breccia (block-in-matrix). Clasts are angular to sub-rounded, pebble to boulder size. Clast composition varies from calcarenites and calcirudites, to marls and marly-calcarenites, all of which crop out in the nearby Hyblean Plateau. The matrix is largely sandy, with a minor silt fraction containing frequent mollusc shells (pectinids and oyster remains). Breccia displays loose (mostly) to moderate (rarely) calcareous cementation, which is occasionally hard. It is mostly structureless, with coarse sub-horizontal to gently dipping (up to 20–30°) parallel bedding and lamination with lateral terminations on erosional surfaces, which outline lenses of coarser clasts in the matrix. Rare gross coarsening-up and clasts imbrications are observed. The sedimentary fabric and metre- to decametre-scale structure of the breccia is highly variable across the study area, and we do not observe trends or preferential distribution of the fabric.

Below the breccia, three units were observed: (i) White-grey biogenic calcarenites rich in quartz, feldspars, molluscs and echinoids. Among foraminifera, benthic species reach values between 80% and 95%, with abundant individuals of *Elphidium*, *Ammonia*, *Gyroidina*, *Asterigerinata*, *Bolivina*. Planktonic foraminifera oscillate between 5% and 20%, with few specimens of *Neogloboquadrina acostaensis*, *Globigerina bulloides* and *Dentoglobigerina* spp. (Supplementary Fig. 5). Applying the regression formula of van der Zwaan et al.[36], a palaeodepth for neritic environments (between 40 and 70 m) was inferred. This unit is upper Tortonian (9.4–7.2 Ma) in age and coeval with the uppermost part of the Tellaro Formation (cfr. Siracusa Member[30]). (ii) Yellow-brown calcarenites rich in fragments of molluscs (*Pecten vigolensis*, *Anadara turonica*, *Parvamussium* sp. and *Ostrea* sp.), echinoids, and bryozoans, and clasts of quartz and feldspar (Supplementary Fig. 5). Among the microfossils, *Ammonia* is the dominant genus, whilst ostracods associated with brackish environments are also present. This unit is upper Tortonian in age and interpreted as similar to the Carrubba Formation described in the eastern part of the Hyblean Plateau, which is a heteropic facies of the Siracusa Member[37]. (iii) White sandy marlstone, displaying cyclic alternation with grey marls, red laminates and whitish pseudo-diatomitic laminates, passing upwards to carbonatic laminated limestones. The marls are rich in planktonic foraminifera with values higher than 85–90% (*Globigerina bulloides*, *Turborotalita quinqueloba*, *T. multiloba*, *Neogloboquadrina acostaensis*, *Orbulina universa*, *Globigerinoides quadrilobatus*), whereas the benthic foraminiferal assemblages include stress tolerant species of dysoxic conditions as *Bulimina echinata*, *B. aculeata*, *B. elongate* and *Bolivina dentellata* (Supplementary Fig. 5). In the red laminates and in the whitish pseudo-diatomitic beds, planktonic microfossils are very abundant and benthic species are only sporadically presents. This is due to the anoxic conditions in the deep water column. These are characteristic of the uppermost part of the Messinian Tripoli Formation (7.05–5.97 Ma)[38,39] (Fig. 3c, d). A unit comprising brecciated whitish marly limestones, rich in oogons of *Chara* sp., lies discordantly above the Tripoli Formation. These lithologies are truncated at the top by the breccia unit. The oogons belong to Charophyta that are typical algae of brackish environment and that have already been described in other Late Messinian Lago-Mare units[3] (Fig. 3d). The unit overlying the breccia is only locally visible. It comprises white marly/silty limestones containing *Sphaeroidinellopsis dehiscens*, *Neogloboquadrina acostaensis*, *Globigerinoides quadrilobatus* and *Globigerina bulloides*, with *Siphonina reticulata* and *Globorotalia margaritae* in the upper section (Supplementary Fig. 5). This unit is interpreted as the Trubi Formation (Fig. 3d). These microfossil assemblages confirm the MPl 1 and MPl 2 biozones, which correspond to the earliest part of the Zanclean[40] (MPl1 biozone: 5.33 – 5.13 Ma; MPl 2 biozone: 5.1–5.0 Ma) (Supplementary Fig. 5). In this unit, planktonic foraminifera reach values higher than 60%, suggesting an upper part of the bathyal environment between 300 and 400 m depth. Our observations contrast with the previous interpretation of the breccia as Quaternary in age[37].

Two types of soft sediment deformation structure are observed at metre- to decametre-scales in some of the outcrops. In the breccia and the underlying Messinian basement there are common soft-sediment deformation structures comprising metre-scale buckle folding, mostly asymmetric and occasionally overturned. The folding is disharmonic in strata with different competence, and deformation bands can be observed in yellow Miocene calcarenites (Fig. 4c, d). Exclusively in the breccia,
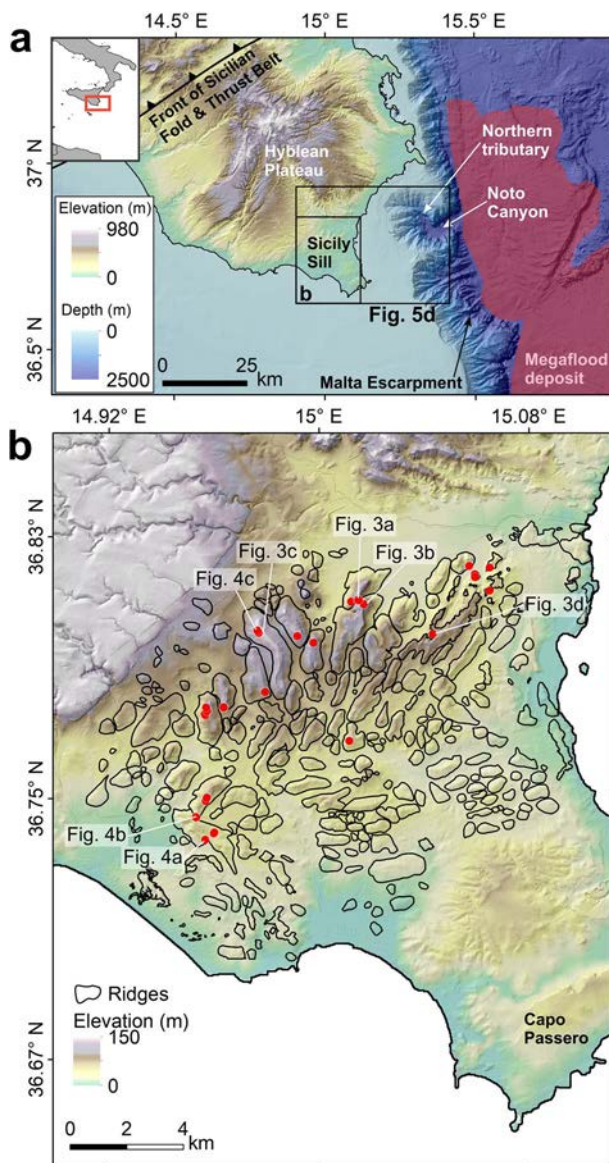
Fig. 1 | Location map. a Location map and digital elevation model of SE Sicily and adjacent seafloor (sources: SITR, EMODnet). The front of the Sicilian Fold and Thrust Belt, the Malta Escarpment, Noto Canyon, and the inferred buried megaflood deposit are labelled. **b** Digital elevation model of the Sicily Sill with outlines of the bases of the ridges. Sampled sites are denoted by red dots.

sedimentary injections occur as sub-vertical or high angle fractures filled with a higher proportion of fine-grained matrix and clasts of the same composition as the surrounding unit (Fig. 4a, b). The fracture fill does not display flow structures. In addition, there are shear bands in the matrix surrounding larger boulders and broken intraclasts embedded in the breccia unit.

Buried erosional shelf channel

Shore parallel and perpendicular seismic reflection profiles from the continental shelf east of the Sicily Sill and west of the upper sections of Noto Canyon reveal a prominent high-amplitude reflector, which represents an erosional unconformity over large sections (Fig. 5a–c). The age of the overlying seismic units is not constrained by physical age dating. However, the low-reflectivity seismic facies directly above the high-amplitude reflection resemble well-known facies of the lower Pliocene from the eastern and western Mediterranean[41–43]. Strata above the low-reflective unit comprise a lower aggrading and upper prograding sedimentary unit with channel-fill

geometries (Fig. 5a, b). These geometries are observed below the inner shelf and the contourite drift geometries below the shelf edge. Following the analogous Plio-Pleistocene sequence described at the base of the Malta Escarpment, we interpret the unconformity between the lower aggrading and upper prograding units as a consequence of the mid-Pleistocene Transition[44,45], when the 100 ka ice age cycles were established and global sea- and base-level dropped by more than 100 m during glacial maxima. Consequentially, the unconformity is named the mid-Pleistocene unconformity (MPU) (Fig. 5a, b). These lines of evidence suggest that the high-amplitude reflector dates back to the Zanclean at the very least, which leads us to interpret it as the Margin Erosional Surface (MES)[1].

The depth of the Margin Erosional Surface varies from a few metres below the seafloor close to the coast, to approximately 700 m below the flanks of Noto Canyon (Fig. 5d). Upslope of Noto Canyon, the Margin Erosional Surface features a 8–20 km wide and up to 270 m deep W-shaped channel, which gently dips from the coastline east of the ridges onshore, towards the lower slope into the head of Noto Canyon (Fig. 5a, b, d). A shorter 5 km wide and 100 m deep U-shaped channel is located 5 km to the north and dips into the northern tributary of Noto Canyon. The base of these channels is highly irregular and shows truncations of the underlying strata (Fig. 5c). Localised, sharp vertical offsets in both dip and strike directions point to uplift along faults at the centre of the larger channel (Fig. 5a), and accounts for the transformation from a presumed original U-shaped to the current W-shaped cross-section.

Hydrodynamic modelling

We perform 2D planform, vertically-averaged, hydrodynamic modelling of the Zanclean megaflood across the Sicily Sill for two scenarios—(i) prior to the formation of the shelf channel and the Noto Canyon on the Malta Escarpment (pre-Noto scenario), and (ii) after their formation (post-Noto scenario)—to estimate flow properties of the megaflood and their evolution. We set different levels for the overspilling western Mediterranean (z_w). Because the sill is at an elevation of 25 m, there is no water flow for $z_w < 25$ m. The flow of water over the sill increases from 0.76 Sv for $z_w = 50$ m (pre-Noto scenario) to 20.8 Sv for $z_w = 100$ m (post-Noto scenario) (Supplementary Fig. 6). The calculated Froude number is sub-critical in most of the model domain and supercritical in the upper shelf channel.

Figure 6 shows two representative stages of the Zanclean megaflood - before ($z_w = 70$ m) and after ($z_w = 90$ m) the formation of the shelf channel and Noto Canyon. Prior to the formation of these two features, the maximum velocity, discharge and shear stress in the study area are estimated at 20 m s^{-1}, 4.1 Sv, and 2.3 kPa, respectively. After the formation of the canyon, these increase to 32 m s^{-1}, 13.0 Sv and 6.5 kPa, and a clockwise change in flow direction is observed.

Discussion

Based on the field observations, we propose that the elongated ridges, the breccia unit and associated deformation structures, and the buried erosional shelf channel were formed by the passage of the Zanclean megaflood from the western to the eastern Mediterranean Basin across a shallow-water marine corridor in SE Sicily at the Messinian-Zanclean boundary (Fig. 7b). The ridges (Fig. 1b) are streamlined landforms compatible with large-scale, turbulent water flow with a predominant NE direction[46–48], which inundated and eroded a planar surface of lower to upper Messinian formations (Fig. 7c, e). The ridges are primarily erosional remnants. The upper portions of the ridges responded more rapidly to both initial erosion and subsequent deposition along the ridge crestline and are thus more readily streamlined by the flow. In contrast, the greater bulk off the base of the ridge is affected by more two-dimensional flows of the same duration running along each flank, giving rise to erosion but with no opportunity for deposition. Such incision of a planar surface to form grooves separating ridges is common across a range of geophysical flow scales, resulting in spiralling erosive flow within the grooves and deposition on the ridge tops[49,50] (Fig. 7c). Streamlined ridges have been documented in other proven Pleistocene catastrophic flood terrains[51–53]. The poor degree of streamlining of some ridges in our study
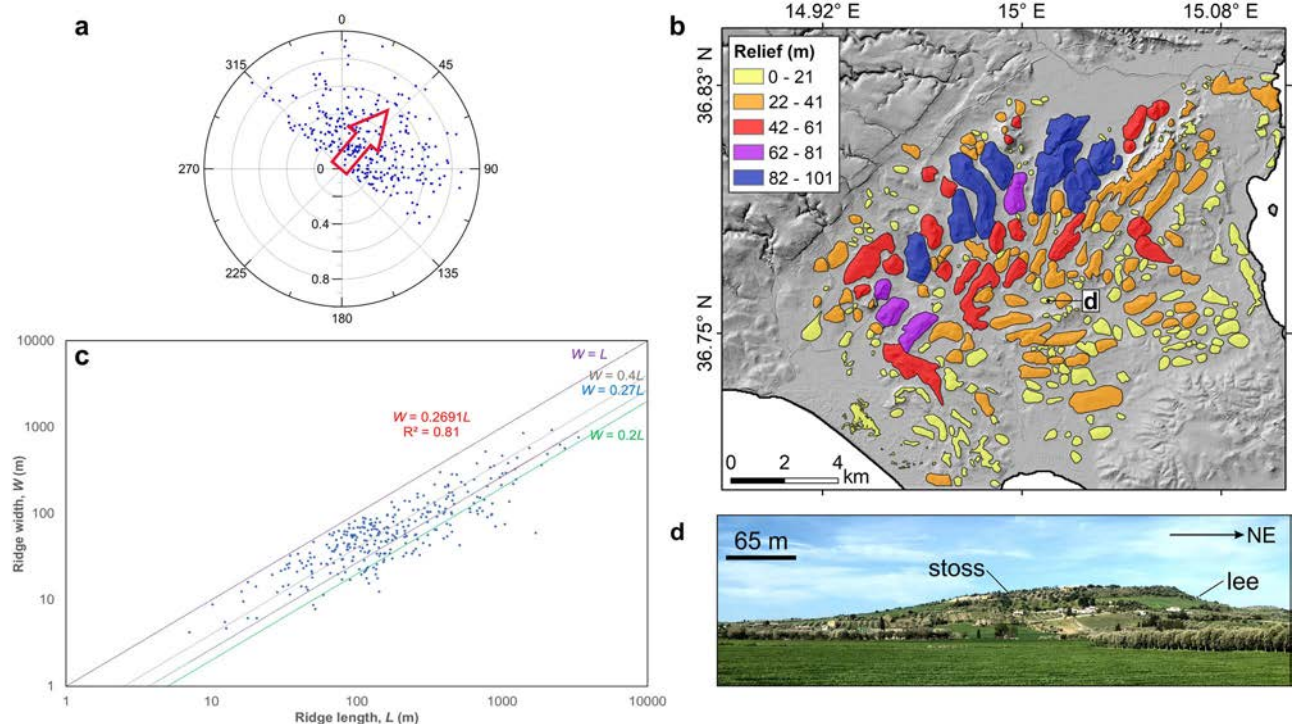
Fig. 2 | Ridge morphology. a Rose plot of the circular orientation (in °) of the long axes of the ridge tops. Aspect ratio is denoted by the radial axis. Red arrow denotes mean orientation. **b** Map of bounding areas around ridges, with colour indicative of ridge relief. Lower *W/L* ratios imply a greater degree of streamlining. **c** Plot of aspect ratio of ridge tops. Aspect ratios of >0.27 for some of the ridge tops point to the occurrence of blockier, poorly streamlined or longer shapes. **d** Profile photograph (taken from the south) of a ridge. Location in figure **b**.

area indicates a relatively short duration of inundation, inadequate to fully streamline the eroding ridges, with dissection of some ridges by cross-flows also resulting in poorly-streamlined landforms[34,35]. The breccia unit consists of material that has been eroded from the ridge flanks and the Hyblean foreland domain by the megaflood, transported as bedload and suspended load, and deposited rapidly along the ridge crests[49,50] (Fig. 7c, e). We attribute the absence of MSC deposits between the Tripoli Formation and the breccia unit to erosion by the megaflood. The emplacement of the breccia unit gave rise to soft-sediment deformation of the unconsolidated Messinian formations. Sedimentary injections, typical of other megaflood deposits[54–56], suggest a marked increase in pore water pressure, which reaches and exceeds the lithostatic load of the recently emplaced breccia. Localised underconsolidation of basal, unlithified formations by the load of rapidly deposited breccia favoured a decrease in effective stress, allowing plastic, soft-sediment deformation in basal layers (e.g[57].; Supplementary Discussion, Supplementary Fig. 1). The alignment of the elongated ridges with the buried erosional shelf channels leading to the Noto Canyon (Fig. 5) confirms that the shelf channels were eroded by the flood and acted as conduits funnelling the flood water and its sediment load from the SE Sicily Sill to the Malta Escarpment, where the Noto Canyon was carved into the lower continental slope. The end-product of this process was the deposition of the ≈1500 km³ chaotic sedimentary deposit at the foot of the slope in the western Ionian Basin[22]. At the end of the megaflood, stable marine conditions favoured pelagic sedimentation during the Zanclean (Trubi Formation) (Fig. 7d).

The field observations also provide insights into the characteristics and evolution of the megaflood. The asymmetry observed in our ridges is characteristic of relatively shallow inundation[58,59], in contrast to the asymmetry of emergent or deeply submerged ridges[60]. By assuming that the highest ridges were submerged, we estimate a conservative value of 20–40 m for the depth of flood inundation above the ridge tops (Fig. 6). A number of observations suggest that the megaflood underwent a change in flow direction (from SW-NE to WSW-ENE) and an increase in velocity. First, the

progressive dissection of a planar surface would be expected to initially produce flat-topped mesas, then elongated ridges, and ultimately streamlined, whaleback landforms[32,61]. The spatial variability in ridge morphology (Fig. 2b)—with shorter, lower and more streamlined ridges in the SE and longer, higher and less streamlined ridges in the NW—is not a result of geological variations[37]. Instead, it indicates that water flow in the SE of the study area, likely situated away from the flood margin, was deeper, stronger and/or more sustained in a WSW-ENE direction. The general change in ridge alignment (Fig. 2b), with the higher ridges oriented N-NNE in the NW and the smaller ridges exhibiting ENE-E orientation in the SE, suggests a clockwise change in flow direction from SW-NE to WSW-ENE as the flood progressed. Second, the top-down or lateral clastic injections observed in the breccia unit can be explained by a process that occurred after the bulk of the volume of the breccia had been deposited. We deduce that this process can be related to an increase in water flow velocity following the deposition of the breccia (Supplementary Discussion, Supplementary Fig. 2). The associated increase in shear stress would have simultaneously produced erosion and clastic injections, where the hydrodynamic component of the flow exceeded the lithostatic pressure in the recently deposited breccias. We infer that changes in megaflood direction and velocity were driven by the formation of the larger shelf channel and Noto Canyon on the Malta Escarpment further downstream, the orientations of which are aligned with the most eastern ridges in SE Sicily (Figs. 1, 2b, 5d). This inference is validated by our hydrodynamic model results (Fig. 6), which show that the excavation of the shelf channel and Noto Canyon, and the increase in the water level, had a noticeable impact in turning the flow direction clockwise and increasing the maximum velocity, discharge and shear stress during the megaflood. The estimated shear stresses far exceed reported critical values for erosion of soft rocks[62] similar to the Tellaro and Tripoli-like formations. Boulders eroded from the deepening troughs between ridges and the shelf channel would have been suspended and comminuted[63] to form a substantial sediment load, which would have lowered erosion thresholds even further.
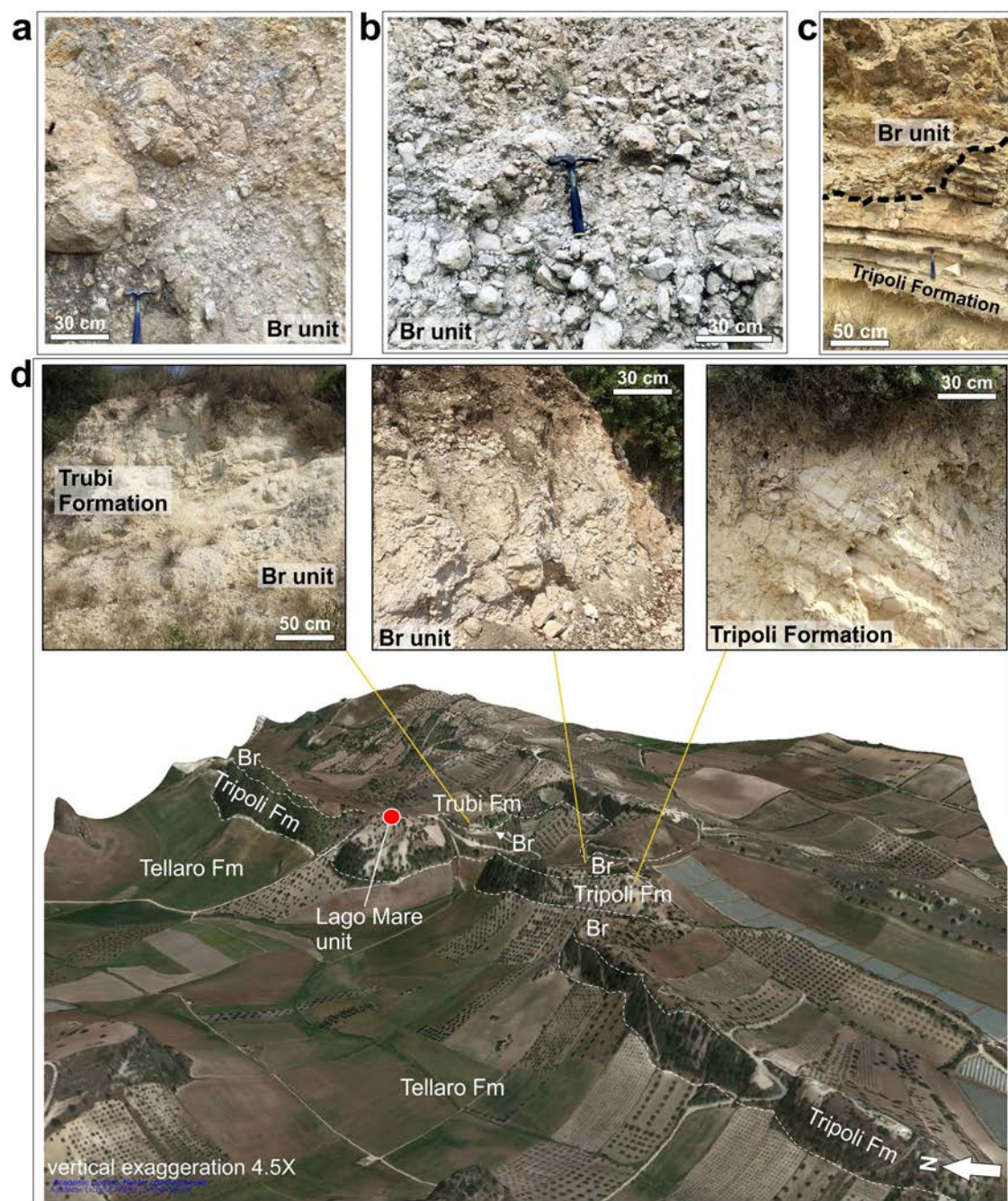
Fig. 3 | Ridge outcrops. a Poorly sorted and clast-supported breccia (Br) unit with polygenic sand matrix and boulder size sub-rounded clasts. **b** Clast-supported breccia with angular monogenic clasts. **c** Erosional surface defining the stratal break-up in the Tripoli Formation overlain by the breccia unit. **d** 3D photomosaic of a ridge with outcrops of the breccia unit, the overlying Trubi and underlying Tripoli Formations (Fm) (Source: Google Earth Image © 2024 Airbus). Locations in Fig. 1.

The volume of rock eroded from the sill (the difference between the pre-Noto and post-Noto topography surfaces) is 2.6 km³. Even if combined with the volume of the larger shelf channel (20 km³) and Noto Canyon (45 km³), the number is too small to explain the megaflood deposit identified in the western Ionian Basin (1430–1620 km³[3[,22]). This observation suggests that most of the deep basin megaflood deposit was eroded and transported from further upstream by the same flood rather than originating from erosion in the modelled area.

Alternative hypotheses to the megaflood hypothesis for the formation of the ridges, breccia unit, and deformation structures include tectonic deformation and fluvial subaerial erosion. Tectonic shortening is an unlikely cause, given the absence of reverse faults at the Sicily Sill, which is situated away from the collisional front (Fig. 1a)[29]. In fact, since the Neogene, this region has been subject to extensional strain, leading to large subsiding corridors in the hanging-wall blocks[64]. The hypothesis of post-MSC subaerial fluvial erosion also appears unlikely; the absence of a distinct fluvial channelled network, the ridge morphologies and the small, localised nature of the catchments argue against this explanation. We also reject the possibility of subaerial fluvial erosion as the cause for the larger shelf channel, in view of its considerable size relative to the largest potential catchment area onshore.

Our study presents limitations regarding the estimation of maximum discharge values from the hydrodynamic modelling. For a water depth (z_w) of 100 m, we observe an additional flow of ≈4 Sv exiting through the southwestern boundary of the computational domain. Obtaining discharges of 100 Sv[11,65] would require modelling a larger domain extended towards the
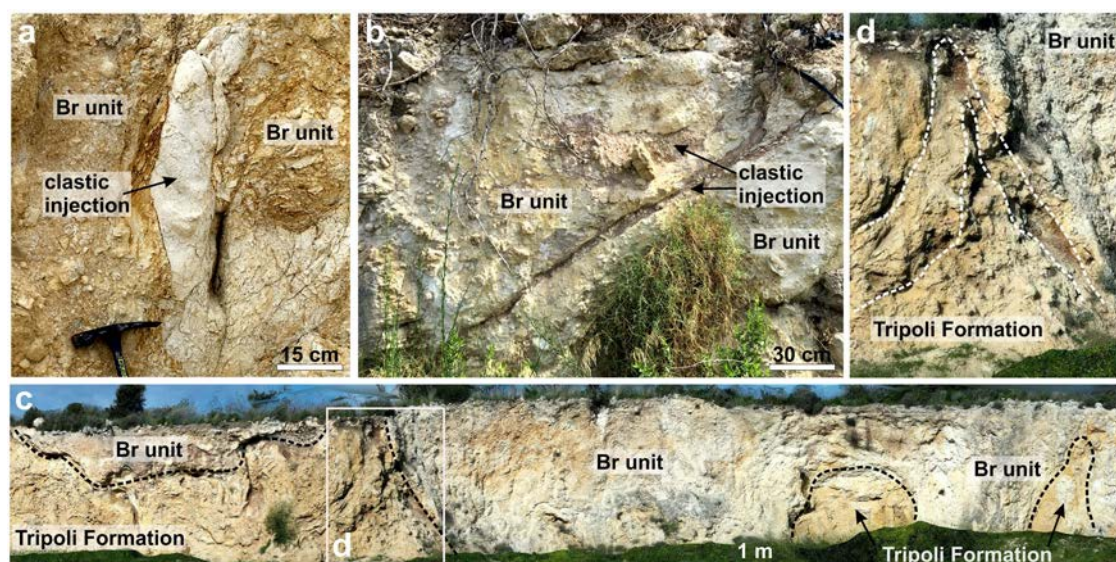
Fig. 4 | Soft-sediment deformation structures and clastic injections induced by the deposition of the breccia (Br) unit. a Vertical clastic (sandy) injection in the breccia unit. **b** Inclined clastic (gravel) injections in the breccia unit. **(c)** Soft-sediment deformation in the Tripoli Formation overlain by the breccia unit (with enlarged boundary between breccia unit and Tripoli Formation shown in **d**). Locations in Fig. 1.

south. We did not consider this because of uncertainties surrounding the palaeogeography of the central Mediterranean region at the end of the MSC, and the lack of field evidence indicating the presence of additional southern gateways.

This study provides the most compelling evidence yet for the largest megaflood postulated to have occurred on Earth, which led to the cataclysmic refilling of the Mediterranean at the termination of the MSC. We present the first large-scale evidence, in the form of erosional ridges topped by breccia deposits, for the passage of the Zanclean megaflood across the Sicily Sill during the overflow from the western to the eastern Mediterranean. This evidence is reinforced by geophysical evidence of a buried shelf channel that connected these onshore, upstream erosional and depositional indicators to the Noto Canyon and the buried chaotic sedimentary body in the western Ionian Basin. Numerical models reveal the crucial role played by the erosion of shelf channel and Noto Canyon in increasing the velocity and stabilising the direction of water flow as the megaflood overtopped the Sicily Sill. Our findings imply substantial (km-scale) lowering of the Mediterranean sea-level prior to the Zanclean megaflood[11]. Furthermore, they indicate that the geologic and geomorphic indicators of the megaflood have persisted in the subaerial and marine record for more than 5 Ma. This conclusion implies that it may be worthwhile to search for additional evidence of the megaflood along the margins of the Mediterranean.

Methods
Field data
Field observations, photographs and samples were collected during fieldwork carried out in SE Sicily in March and September 2023. These data were complemented by a digital elevation model (LiDAR, 2 m grid size, collected in 2008) and aerial photographs (15 cm grid size, collected in 2018) available from the Geoportal Regione Sicilia (https://www.sitr.regione.sicilia.it/).

Ridge mapping and geomorphometric analyses
The publicly available datasets were uploaded in a Geographic Information System. The bases of the ridges were delineated by extracting profile curvature and identifying continuous concave breaks of slope. A polygon was drawn along lines of high profile curvature where the adjacent slope gradient was >5°. The same was done for the top using a convex break of slope. Bounding boxes were generated for each ridge, from which the ridge length, width and the bearing of the long axis were measured. A trough depth map was extracted using hydrology tools[66]. The deepest values between ridges

were extracted and interpolated to generate a smooth surface across the deepest sections of the troughs. The original digital elevation model was subtracted from this interpolated surface, and the highest value of relief was extracted for each ridge.

Geological sample analyses
To determine the stratigraphic ages of the lithological units present in the studied area, 73 samples were collected above and below the breccia unit (Fig. 1b). In the outcrops where the stratigraphic units were thicker than 2 m, a sampling interval of 50 cm was used. From each sample, 30 g of dried sediment were washed through a 63 μm sieve and dried to 40 °C. All samples were subject to micropaleontological analysis by identifying the foraminiferal assemblages. Thin sections were prepared for analysing microfacies and to determine the mineralogical composition to discriminate the lithologies. The foraminiferal identification was based on a qualitative analysis carried out on the >63 and >125 μm fractions. For this study, the planktonic foraminiferal biostratigraphic scheme proposed by ref. 40 was used. For benthic foraminifera, the classifications by refs. 67,68 were used.

Marine geophysical survey
The seismic profiles were acquired during the M199 (DELUGE) cruise[69] on board the *R/V Meteor* in February-March 2024. The data set consists of over 1400 profile kilometres. The seismic source was a 6-tip Applied Acoustic Delta Sparker with a shot interval of 7 s. The streamer was a 500 m, 120 channel digital streamer (4.2 m channel spacing, near-offset of 110 m). Despite having a dominant frequency of around 150 Hz (dominant wavelength of ≈10 m at the seafloor), the maximum vertical resolution of the data is ≈20 m due to the double pulse generated by the source. The processing sequence included: (1) resampling from 0.5 ms to 1 ms, (2) crooked line common mid-point binning (10 m bin spacing), (3) semblance velocity analysis (2.5 km spacing), (4) spherical divergence correction, (5) shot domain threshold median noise attenuation, (6) normal move-out correction using 2–30° angle mute and fold-compensated stacking, (7) finite difference migration, (8) post-stack targeted F-K de-multiple sequence (to suppress the first and second water bottom residual multiple energy), and (9) F-X deconvolution, followed by a 35-45-300-400 Hz Ormsby bandpass filter (zero-phase) and a top mute above the water bottom. Depth conversion of the Margin Erosional Surface was performed by assuming a seismic velocity of 1.8 km s^{-1} in the overlying sediments and 1.5 km s^{-1} in the water column.

Fig. 5 | Buried erosional shelf channels upslope of Noto Canyon. a Part of seismic reflection profile HH24-03 illustrating a cross-section of the larger erosional shelf channel. **b** Part of seismic reflection profile HH24-29 showing a dip section along the larger erosional shelf channel. Both (**a**) and (**b**) display the location of the mid-Pleistocene unconformity (MPU). Inset (**c**) shows truncated reflectors in seismic reflection profile HH24-05. TWT = two-way travel time; VE = vertical exaggeration. Locations of profiles in Figure (**d**). **d** Interpolated sub-seafloor depth of the MES across the continental shelf east of the Sicily Sill and upslope of Noto Canyon, outlining the two erosional channels. White arrows denote inferred direction of water flow. Digital elevation model of SE Sicily and hill-shade map of the adjacent seafloor are also shown.
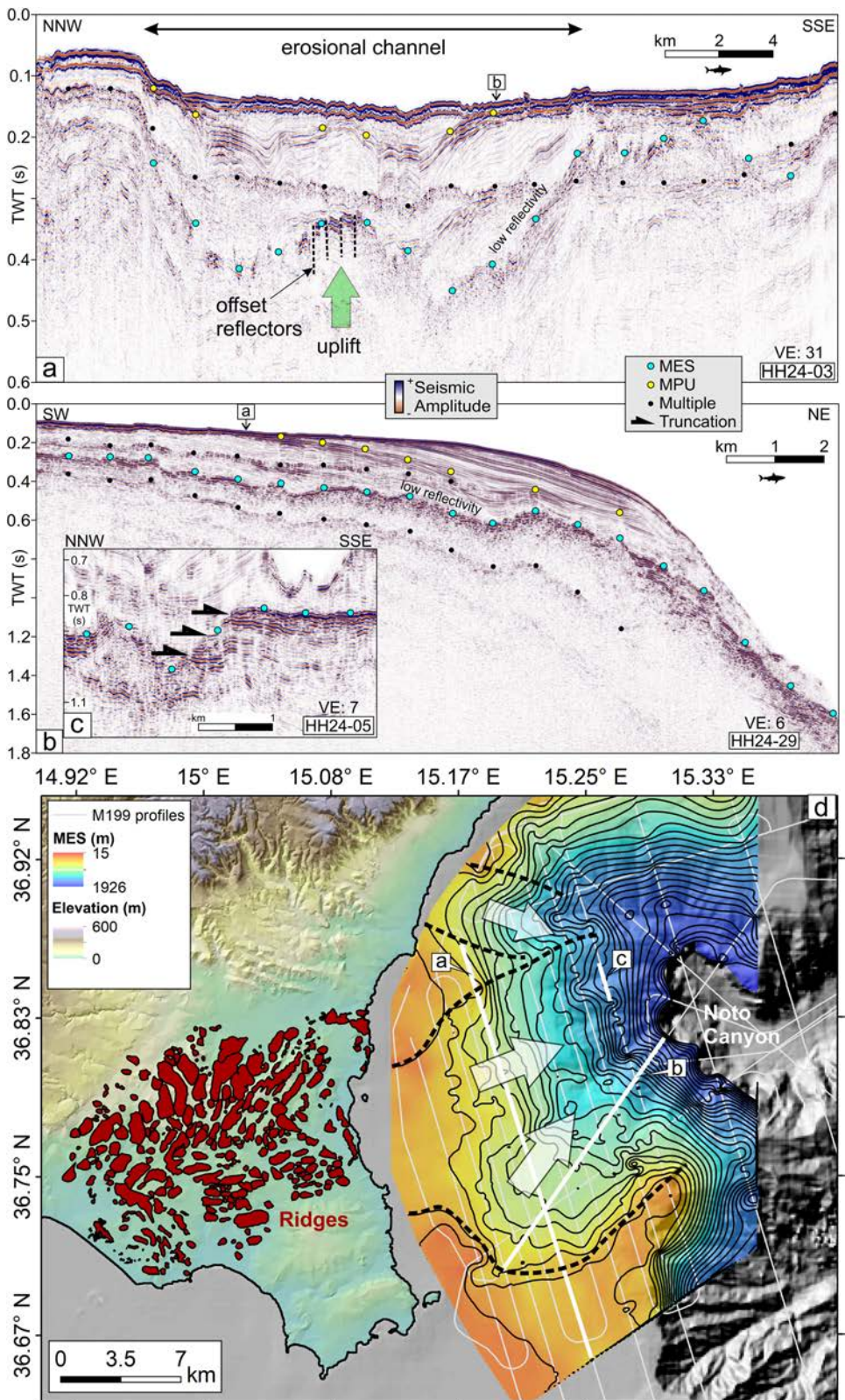
Numerical modelling

The topographic reconstructions used as pre-Noto and post-Noto scenarios in the numerical model have been made based on present topography/bathymetry grids with a cell size of 100 m. For the post-Noto scenario, the grids were modified to remove the overlying Plio-Pleistocene sediments (as interpreted in ref. 22), expose the larger shelf channel upslope of Noto Canyon, and infill the northern tributary of Noto Canyon (which is inferred to have been formed by slope failure during the Pleistocene[23]) by linearly interpolating across the canyon tributary rim. To restore the southwards tilting of the southern flank of the Hyblean Plateau related to flexural forebulge uplifting[70], we have tilted the topographic model northwards by 0.3°, which causes the study area to be the lowest pass between the western
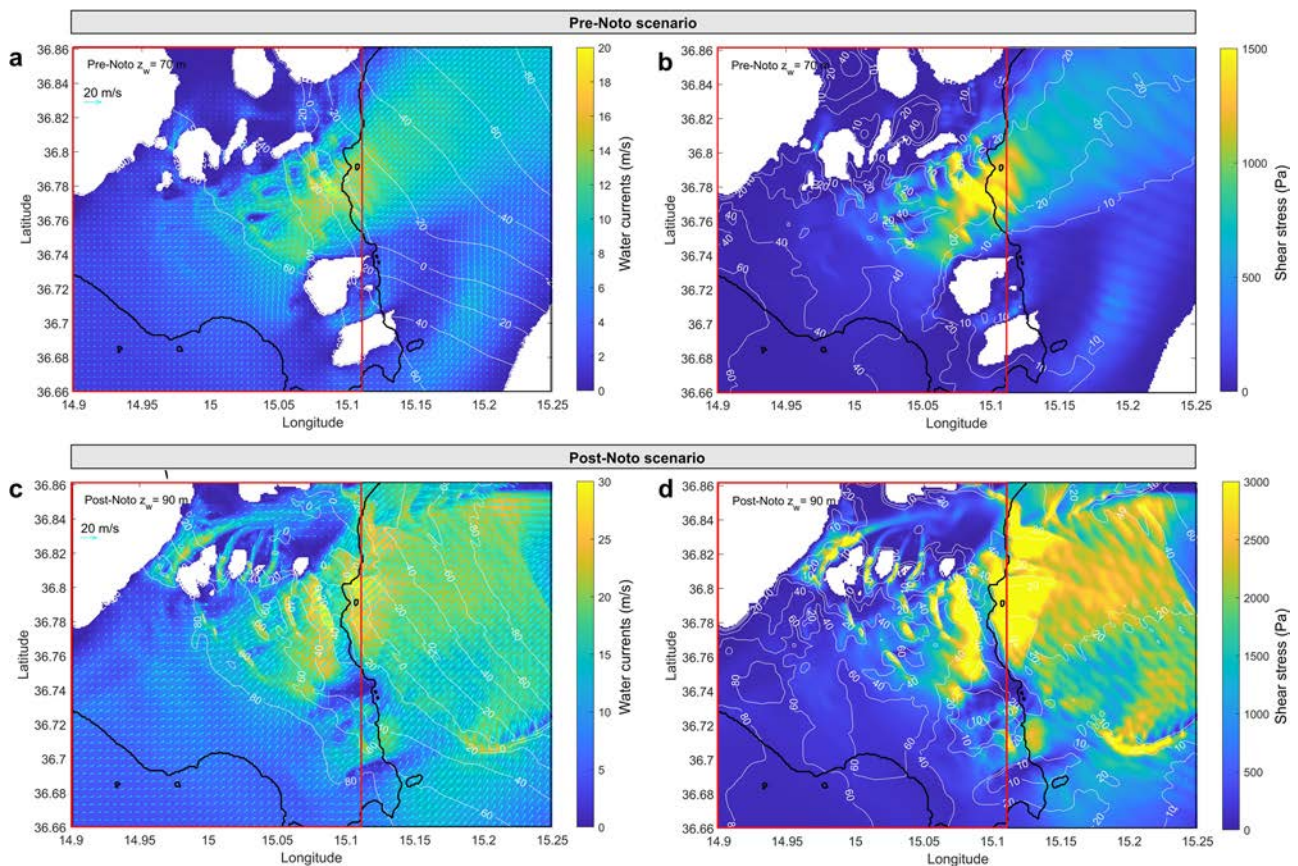
Fig. 6 | Results of the 2D hydrodynamic model. Modulus (colour-bar scale) and vector field of water velocity, and free surface elevation (contours in m) (left panels), and bottom shear stress (colour-bar scale) and water depth (contours in m) (right panels) for the pre-Noto (**a**, **b**) and post-Noto (**c**, **d**) scenarios. The stated water level in the open western boundary (z_w) is indicated in each panel. The resulting E-W water flow is 4.1 Sv for (**a**, **b**) and 13 Sv for (**c**, **d**) (1 Sv = 10^6 m^3 s^{-1}). The red rectangle corresponds to the area in Fig. 1b.

and eastern Mediterranean within this model domain. For the pre-Noto scenario, starting from the post-Noto grid, we have fully infilled the shelf channel and Noto Canyon, and raised the topography of the ridges area by following a smooth envelope following the ridge tops, using linear interpolation in both cases. The latter was intended to reconstruct relief prior to the megaflood erosion. These reconstructions are somewhat speculative due to the lack of constraints on the 3D continuity of the buried part of the Noto Canyon or the amount of erosion that occurred above the present ridge topography. Therefore, it must be kept in mind that their purpose is primarily to test the different flow conditions expected before and after the formation of the shelf channel and Noto Canyon, and compare them with the ridge morphometry.

The numerical model is based on 2D depth-averaged barotropic hydrodynamic equations and includes a wet/dry algorithm that continuously updates the computational domain. The numerical code, developed at the University of Seville[71], has been shown to be a robust computational tool to deal with cataclysmic floods (e.g., the Zanclean megaflood[65]; the late Pleistocene Lake Bonneville flood[72]). It has been adapted for the present study with the pre-Noto and post-Noto topographic grids, with a domain covering 14.7617°–15.5844°E in geographical longitude and 36.4345°–36.9516°N in latitude.

For the friction coefficient, k_f, we adopted the formulation of[72,73] as a function of the water depth, d, and the Manning coefficient n, as $k_f = gn^2 d^{-1/3}$, with g being the acceleration of the gravity. A uniform value of $n = 0.04$ has been selected for this study, similar to the other applications of 2D-hydrodynamic models for outburst floods: $n = 0.05$ (Lake Kuray–Chuja[74]), $n = 0.04$–0.05 (for valley floor and step margins, Missoula floods[75]), or $n = 0.03$–0.05 (Bonneville Lake[72]). The sensitivity of our model output to the selection of the Manning coefficient has been assessed.

The boundary conditions were set as follows: (i) no flow through the emerged terrain; (ii) a gravity wave radiation condition in the open north and east boundaries; (iii) uniform and constant water elevation in the open western boundary, z_W (which forces a W-E flow); (iv) a null gradient condition in the open south boundary.

As initial conditions, we used uniform water levels in the Ionian Basin, Z_{IB}, and allowed the inundation of the domain west of the sill with the water level z_W. The numerical simulation was initialised with still waters and allowed the flow to find its path through the dry terrain to reach a quasi-steady state for the specified boundary condition (which provides a picture of the stage of the flood). It is worth noting that Z_{IB} had no effect on the water flow when it remained lower than the Malta Escarpment. Thus, the ascribed values (500 m and 100 m below the grid datum) for the pre-Noto and post-Noto scenarios only provided qualitative information on the stage of the Zanclean megaflood.

A series of runs was performed for the pre-Noto scenario with z_W values of 50, 60 and 70 m, while we used z_W values of 70, 80, 90 and 100 m for the post-Noto scenario. This approach provides a gross picture of the temporal evolution of the flood, as shown in Supplementary Fig. 6. To enhance convergence and speed up the process, the fields of water elevation and water current from a steady state were used as initial conditions for a subsequent stage with a higher water level at the western boundary.

The model generates spatial maps with the elevation of the free surface of the water, water depths, current vectors, bottom shear stress, friction coefficient, and Froude number, as well as time series of the W-E water flow and of any of the above parameters at selected stations within the domain.

Using a Manning coefficient $n = 0.05$ instead of 0.04 results in a reduction of ≈15% in water velocity, shear stress and discharge without changing the main features of the flow reported in Supplementary Fig. 6.

Fig. 7 | Idealised schematic conceptual model. Model for the formation of the shelf channel, elongated ridges, breccia unit and associated deformation structures by the Zanclean megaflood across the Sicily Sill. **a–d** 2D cross-section of the Sicily Sill at different stages. Figure **c** and **e** represent the same stage. The flow of the water in figure (**c**) is away from the reader. The tilt in figure **d** is a result of the uplift of the Hyblean Plateau.
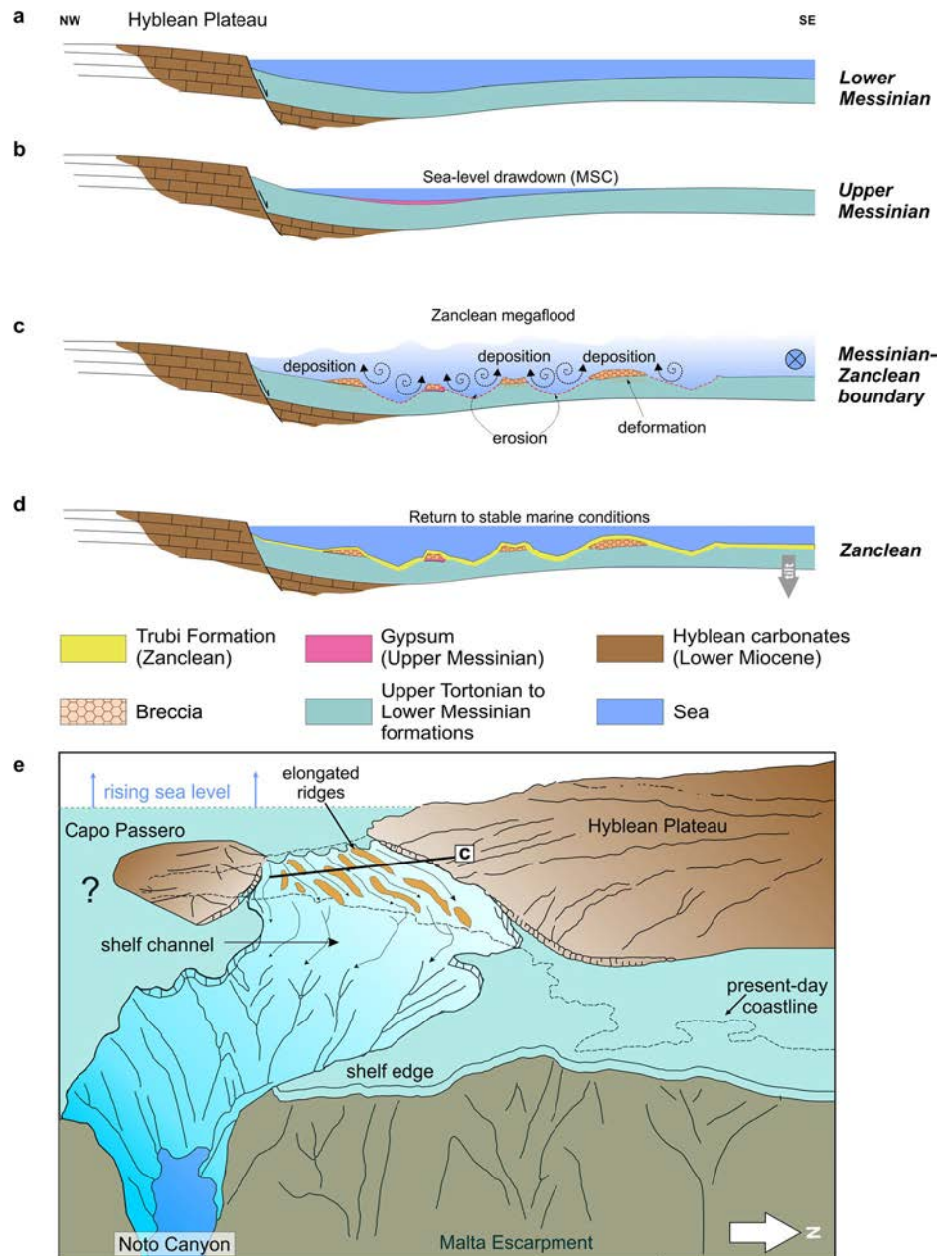
The erosive power of the flow progressively diminishes as the water level in the eastern Mediterranean exceeds the depth of the sill.

Data availability
All data needed to evaluate the conclusions in the paper are present in the paper and/or the Supplementary Materials. Processed seismic reflection profiles are available via this link https://zenodo.org/doi/10.5281/zenodo.10818062. Samples and photographs are available upon request from Antonio Caruso (antonio.caruso@unipa.it). A list of the samples is available via this link (https://doi.org/10.58052/IEZAN0001 to https://doi.org/10.58052/IEZAN0022). Numerical model results are available via this link https://zenodo.org/records/10839752?token=eyJhbGciOiJIUzUxMiIsImlhdCI6MTcxMDg2NjIyMiwiZXhwIjoxNzE4NzU1MTk5fQ.eyJpZCI6ImRkMjg4MjIxLWFkOGQtNDIc0OS04ZWZmLWZmZTUxNDhmM2FmNyIsImRhdGEiOnt9LCJyYW5kb20iOiIyYmM3ZGE4MTYwZmI1MTZZmNjliYjY0ZWI2OGI3ZCJ9.GPZ_Ogsl5MaTiE5-QcJutUhWC0r76VtvyXxRJACMzUs3lK2OnKPHb089T-SyRJfqG-L0o2R_hqZ5iBIxdZdqvw.

Code availability
The code for the hydrodynamic model is available via this link https://doi.org/10.5281/zenodo.13897180.

References
1. Lofi, J. et al. *Seismic Atlas of The "Messinian Salinity Crisis" markers in the Mediterranean and Black Seas*. (2011).
2. Hsü, K. J., Ryan, W. B. F. & Cita, M. B. The Late Miocene desiccation of the Mediterranean. *Nature* **242**, 240–244 (1973).
3. Rouchy, J. M. & Caruso, A. The Messinian salinity crisis in the Mediterranean basin: A reassessment of the data and an integrated scenario. *Sediment. Geol.* **188-189**, 35–67 (2006).
4. Roveri, M. et al. The Messinian Salinity Crisis: Past and future of a great challenge for marine sciences. *Mar. Geol.* **352**, 25–58 (2014).

5. Ryan, W. B. F. 50th anniversary review of the Mediterranean desiccation hypothesis. *La Riv. del. Nuovo Cim.* **46**, 163–291 (2023).

6. Ryan, W. B. F. Decoding the Mediterranean salinity crisis. *Sedimentology* **56**, 95–136 (2008).

7. Haq, B., Gorini, C., Baur, J., Moneron, J. & Rubino, J.-L. Deep Mediterranean's Messinian evaporite giant: How much salt? *Glob. Planet. Change* **184**, 103052 (2020).

8. Krijgsman, W. et al. Causes and consequences of the Messinian salinity crisis. *Nat. Rev. Earth Environ.* **5**, 335–350 (2024).

9. Cita, M. B. & Ryan, W. B. F. Vol. 124 1405-1415 (Milan, Università, Istituto di Geologia e Paleontologia, 1972).

10. Hsü, K. J., Cita, M. B. & Ryan, W. B. F. in *Initial Reports of the Deep Sea Drilling Project* Vol. 13 (eds W.F. Ryan, et al.) 1023-1231 (1973).

11. Garcia-Castellanos, D. et al. The Zanclean megaflood of the Mediterranean – Searching for independent evidence. *Earth-Sci. Rev.* **201**, 103061 (2020).

12. Blanc, P. L. The opening of the Plio-Quaternary Gibraltar Strait: Assessing the size of a cataclysm. *Geodinamica Acta* **15**, 303–317 (2002).

13. Garcia-Castellanos, D. et al. Catastrophic flood of the Mediterranean after the Messinian salinity crisis. *Nature* **462**, 778–781 (2009).

14. Abril, J. M. & Periáñez, R. Revisiting the time scale and size of the Zanclean flood of the Mediterranean (5.33Ma) from CFD simulations. *Mar. Geol.* **382**, 242–256 (2016).

15. Garcia-Castellanos, D. & O'Connor, J. E. Outburst floods provide erodability estimates consistent with long-term landscape evolution. *Sci. Rep.* **8**, 10573 (2018).

16. Carling, P. et al. Unsteady 1D and 2D hydraulic models with ice dam break for Quaternary megaflood, Altai Mountains, southern Siberia. *Glob. Planet. Change* **70**, 24–34 (2010).

17. Van Couvering, J. A., Castradori, D., Cita, M. B., Hilgen, F. J. & Rio, D. The base of the Zanclean Stage and of the Pliocene Series. *Episodes* **23**, 179–187 (2000).

18. Caruso, A., Blanc-Valleron, M. M., Da Prato, S., Pierre, C. & Rouchy, J. M. The late Messinian "Lago-Mare" event and the Zanclean Reflooding in the Mediterranean Sea: New insights from the Cuevas del Almanzora section (Vera Basin, South-Eastern Spain). *Earth-Sci. Rev.* **200**, 102993 (2020).

19. Amarathunga, U. et al. Sill-controlled salinity contrasts followed post-Messinian flooding of the Mediterranean. *Nat. Geosci.* **15**, 720–725 (2022).

20. Estrada, F. et al. Impact of pulsed Atlantic water inflow into the Alboran Basin at the time of the Zanclean flooding. *Geo-Mar. Lett.* **31**, 361–376 (2011).

21. Periáñez, R., Abril, J. M., Garcia-Castellanos, D., Estrada, F. & Ercilla, G. An exploratory modelling study on sediment transport during the Zanclean flood of the Mediterranean. *SN Appl. Sci.* **1**, 364 (2019).

22. Micallef, A. et al. Evidence of the Zanclean megaflood in the eastern Mediterranean Basin. *Sci. Rep.* **8**, 1078 (2018).

23. Spatola, D. et al. A single-stage megaflood at the termination of the Messinian salinity crisis: Geophysical and modelling evidence from the eastern Mediterranean Basin. *Mar. Geol.* **430**, 106337 (2020).

24. van Dijk, G. et al. A terminal Messinian flooding of the Mediterranean evidenced by contouritic deposits on Sicily. *Sedimentology* **70**, 1195–1223 (2023).

25. Pilade, F. et al. Deciphering the termination of the Messinian salinity crisis: The alkenone record of the Miocene-Pliocene transition in the northern Mediterranean. *Palaeogeogr., Palaeoclimatol., Palaeoecol.* **631**, 111831 (2023).

26. Merzeraud, G. et al. Sedimentology and sequence stratigraphy of the late-Messinian - Early pliocene continental to marine deposits of the Boudinar basin (North Morocco). *J. Afr. Earth Sci.* **150**, 205–223 (2019).

27. Roveri, M., Lugli, S. & Manzi, V. The Desiccation and Catastrophic Refilling of the Mediterranean: 50 Years of Facts, Hypotheses, and Myths Around the Messinian Salinity Crisis. *Ann. Rev. Marine Sci.* **17**, https://doi.org/10.1146/annurev-marine-021723-110155 (2024).

28. Marzocchi, A., Flecker, R., Van Baak, C. G., Lunt, D. J. & Krijgsman, W. Mediterranean outflow pump: An alternative mechanism for the Lago-mare and the end of the Messinian Salinity Crisis. *Geology* **44**, 523–526 (2016).

29. Henriquet, M., Dominguez, S., Barreca, G., Malavieille, J. & Monaco, C. Structural and tectono-stratigraphic review of the Sicilian orogen and new insights from analogue modeling. *Earth-Sci. Rev.* **208**, 103257 (2020).

30. Lentini, F. & Carbone, S. in *Descriptive Memories of the Geological Map of Italy* Vol. XCV (eds F. Lentini & S. Carbone) 31-98 (ISPRA-Servizio Geologico d'Italia, 2000).

31. Micallef, A. et al. Geomorphic evolution of the Malta Escarpment and implications for the Messinian evaporative drawdown in the eastern Mediterranean Sea. *Geomorphology* **327**, 264–283 (2019).

32. Halimov, M. & Fritz, F. Eight yardang types in Central Asia. *Z. f. ür. Geomorphologie* **33**, 205–217 (1989).

33. Fox, R. W. & McDonald, A. T. *Introduction to Fluid Mechanics*. 8th edn, (John Wiley and Sons, 2011).

34. Carling, P. A. Subaqueous "yardangs": Analogs for aeolian yardang evolution. *J. Geophys. Res.: Earth Surf.* **118**, 276–287 (2013).

35. Collier, J. S. et al. Streamlined islands and the English Channel megaflood hypothesis. *Glob. Planet. Change* **135**, 190–206 (2015).

36. van der Zwaan, G. J., Jorissen, F. J. & de Stigter, H. C. The depth dependency of planktonic/benthic foraminiferal ratios: Constraints and applications. *Mar. Geol.* **95**, 1–16 (1990).

37. Carbone, S., Grasso, M. & Lentini, F. (ed Società Elaborazioni Cartografiche) (1984).

38. Tzevahirtzian, A., Caruso, A., Andreetto, F., Bonomo, S. & Krijgsman, W. A bio-chronostratigraphic study of the upper Miocene from the northern Caltanissetta Basin, Sicily (core 3AGN2S04). Implications for dating the Messinian Salinity Crisis onset. *Sediment. Geol.* **445**, 106330 (2023).

39. Kouwenhoven, T. J. et al. Paleoenvironmental evolution of the eastern Mediterranean during the Messinian: Constraints from integrated microfossil data of the Pissouri Basin (Cyprus). *Mar. Micropaleontol.* **60**, 17–44 (2006).

40. Lirer, F. et al. Mediterranean Neogene planktonic foraminifer biozonation and biochronology. *Earth-Sci. Rev.* **196**, 102869 (2019).

41. Flecker, R. et al. Evolution of the Late Miocene Mediterranean–Atlantic gateways and their impact on regional and global environmental change. *Earth-Sci. Rev.* **150**, 365–392 (2015).

42. Ben Zeev, Y. & Gvirtzman, Z. When two salt tectonics systems meet: Gliding downslope the levant margin and salt out-squeezing from under the Nile Delta. *Tectonics* **39**, e2019TC005715 (2020).

43. Maillard, A. et al. New onshore/offshore evidence of the Messinian Erosion Surface from key areas: The Ibiza-Balearic Promontory and the Orosei-Eastern Sardinian margin. *BSGF - Earth Sci. Bull.* **191**, 9 (2020).

44. Mudelsee, M. & Schulz, M. The Mid-Pleistocene climate transition: onset of 100 ka cycle lags ice volume build-up by 280 ka. *Earth Planet. Sci. Lett.* **151**, 117–123 (1997).

45. Rebesco, M. et al. Bottom current-controlled Quaternary sedimentation at the foot of the Malta Escarpment (Ionian Basin, Mediterranean). *Mar. Geol.* **441**, 106596 (2021).

46. Chorley, R. J. The shape of drumlins. *J. Glaciol.* **3**, 339–344 (1959).

47. Baker, V. R. & Kochel, R. C. in *Proceedings of the Ninth Lunar and Planetary Science Conference* (ed R. B. Morrill) 3193-3203 (Pergamon Press, 1978).

48. McCauley, J. F., Grolier, M. J. & Breed, C. S. in *Proceedings of the 8th Annual Geomorphology Symposium* (ed D. O. Doehring) 233-369 (Binghampton, 1977).

49. Carling, P. A., Williams, J. J., Croudace, I. W. & Amos, C. L. Formation of mud ridge and runnels in the intertidal zone of the Severn Estuary, UK. *Continental Shelf Res.* **29**, 1913–1926 (2009).

50. Williams, J. J., Carling, P. A., Amos, C. L. & Thompson, C. Field investigation of ridge–runnel dynamics on an intertidal mudflat. *Estuar., Coast. Shelf Sci.* **79**, 213–229 (2008).

51. Komar, P. D. The Lemniscate Loop: Comparisons with the Shapes of Streamlined Landforms. *J. Geol.* **92**, 133–145 (1984).

52. Kehew, A. E. & Lord, M. L. Origin and large-scale erosional features of Glacial-Lake spillways in the northern Great-Plains. *Geol. Soc. Am. Bull.* **97**, 162–177 (1986).

53. Norris, S. L. et al. Catastrophic Drainage From the Northwestern Outlet of Glacial Lake Agassiz During the Younger Dryas. *Geophys. Res. Lett.* **48**, e2021GL093919 (2021).

54. Smith, G. A. Missoula flood dynamics and magnitudes inferred from sedimentology of slack-water deposits on the Columbia Plateau, Washington. *GSA Bull.* **105**, 77–100 (1993).

55. Baker, V. R., Burr, D. M. & Carling, P. A. *Megaflooding on Earth and Mars*. (Cambridge University Press, 2009).

56. Cooley, S. W. in *Northwest Geology* Vol. 43 133-147 (Tobacco Root Geological Society Guidebook, 2014).

57. van Loon, A. J. Soft-sediment deformation structures in siliciclastic sediments: an overview. *Geologos* **15**, 3–55 (2009).

58. Sadeque, M. A., Rajaratnam, N. & Loewen, M. R. Flow around cylinders in open channels. *J. Eng. Mech.* **134**, 60–71 (2008).

59. Jackson, T. R., Haggerty, R. & Apte, S. V. A fluid-mechanics based classification scheme for surface transient storage in riverine environments: quantitatively separating surface from hyporheic transient storage. *Hydrol. Earth Syst. Sci.* **17**, 2747–2779 (2013).

60. Meinsen, J. et al. Middle Pleistocene (Saalian) lake outburst floods in the Münsterland Embayment (NW Germany): impacts and magnitudes. *Quat. Sci. Rev.* **30**, 2597–2625 (2011).

61. Carling, P. A. Freshwater megaflood sedimentation: What can we learn about generic processes? *Earth-Sci. Rev.* **125**, 87–113 (2013).

62. Sunamura, T. & Matsukura, Y. Laboratory test of bedrock abrasion by sediment-entrained water flow: a relationship between abrasion rate and bedrock strength. *Trans. Jpn. Geomorphological Union* **27**, 85–94 (2006).

63. Carling, P. A. & Fan, X. Particle comminution defines megaflood and superflood energetics. *Earth-Sci. Rev.* **204**, 103087 (2020).

64. Torelli, L., Grasso, M., Mazzoldi, G. & Peis, D. Plio-Quaternary tectonic evolution and structure of the Catania foredeep, the northern Hyblean Plateau and the Ionian shelf (SE Sicily). *Tectonophysics* **298**, 209–221 (1998).

65. Periáñez, R. & Abril, J. M. Computational fluid dynamics simulations of the Zanclean catastrophic flood of the Mediterranean (5.33Ma). *Palaeogeogr., Palaeoclimatol., Palaeoecol.* **424**, 49–60 (2015).

66. Micallef, A., Berndt, C., Masson, D. G. & Stow, D. A. V. A technique for the morphological characterization of submarine landscapes as exemplified by debris flows of the Storegga Slide. *J. Geophys. Res.* **112**, F02001 (2007).

67. Sen Gupta, B. K. & Machain-Castillo, M. L. Benthic foraminifera in oxygen-poor habitats. *Mar. Micropaleontol.* **20**, 183–201 (1993).

68. Loeblich, A. R. & Tappan, H. in *Studies in Benthic foraminifera* (eds Y. Takayanagi & T. Saito) 93-102 (Tokai University Press, 1992).

69. Hübscher, C. et al. Erosional and depositional signatures of the Zanclean megaflood in the central Mediterranean Basin, Cruise No. M199 (GPF 22-1_026), 25.02.2023–11.03.2024, Catania (Italy) – Malaga (Spain). (2024).

70. Henriquet, M. et al. Deep Origin of the Dome-Shaped Hyblean Plateau, Southeastern Sicily: A New Tectono-Magmatic Model. *Tectonics* **38**, 4488–4515 (2019).

71. Periáñez, R. & Abril, J. M. Modeling tsunami propagation in the Iberia–Africa plate boundary: Historical events, regional exposure and the case-study of the former Gulf of Tartessos. *J. Mar. Syst.* **111-112**, 223–234 (2013).

72. Abril-Hernández, J. M., Periáñez, R., O'Connor, J. E. & Garcia-Castellanos, D. Computational Fluid Dynamics simulations of the Late Pleistocene Lake Bonneville Flood. *J. Hydrol.* **561**, 1–15 (2018).

73. Mayo, T., Butler, T., Dawson, C. & Hoteit, I. Data assimilation within the Advanced Circulation (ADCIRC) modeling framework for the estimation of Manning's friction coefficient. *Ocean Model.* **76**, 43–58 (2014).

74. Bohorquez, P. & Darby, S. E. The use of one- and two-dimensional hydraulic modelling to reconstruct a glacial outburst flood in a steep Alpine valley. *J. Hydrol.* **361**, 240–261 (2008).

75. Miyamoto, H. et al. Numerical simulations of large-scale cataclysmic floodwater: A simple depth-averaged model and an illustrative application. *Geomorphology* **76**, 179–192 (2006).

Acknowledgements

Author contributions

G.B. conceived the original idea, which was elaborated with A.M. and A.C. Data collection was carried out by A.M., G.B., A.C., P.C., D.C., A.Car, C.H., J.F., B.H., M.H. and J.P., whereas J.M.A.H. and R.P. performed the numerical simulations. All authors discussed the results and contributed to the final manuscript. A.M. supervised the project.

Competing interests

The authors declare no competing interests.

Additional information

Supplementary information The online version contains supplementary material available at https://doi.org/10.1038/s43247-024-01972-w.

Correspondence and requests for materials should be addressed to Aaron Micallef.

Peer review information *Communications Earth & Environment* thanks Jurgen Herget, Juan Ballesteros-Canovas and the other, anonymous, reviewer(s) for their contribution to the peer review of this work. Primary Handling Editor: Carolina Ortiz Guerrero. A peer review file is available.

Reprints and permissions information is available at http://www.nature.com/reprints

Publisher's note Springer Nature remains neutral with regard to jurisdictional claims in published maps and institutional affiliations.